



Structural, optical, and electrical properties of multi-component P-type oxide-semiconductor Cu-Mn-Sn-O thin films

Dinh The Nam^{a,b}, Bui Nguyen Quoc Trinh^{c,*}

^a Vietnam National University, Hanoi, University of Science, Faculty of Physics, 334 Nguyen Trai, Thanh Xuan, Hanoi, Vietnam

^b Tokyo Institute of Technology, School of Materials and Chemical Technology, Department of Materials Science and Engineering, 2-12-1 Ookayama, Meguro, Tokyo 152-8550, Japan

^c Vietnam National University, Hanoi, Vietnam Japan University, Faculty of Advanced Technology and Engineering, Nanotechnology Program, Luu Huu Phuoc, Nam Tu Liem, Hanoi, Vietnam

ARTICLE INFO

Keywords:

Copper oxide
Multi-component oxide
Solution process
P-type semiconductor
Figure of merit

ABSTRACT

P-type oxide semiconductors have attracted significant attention as conducting channel layers due to their wide applications in electronic devices. In this study, multi-component oxide-semiconductor $\text{Cu}_{1-2x}\text{Mn}_x\text{Sn}_x\text{O}$ thin films with $x = 0.05, 0.10, 0.15, 0.20, 0.25, 0.30$, and 0.33 were prepared on glass substrates using a solution process accompanied by a spin-coating technique. A phase transition between the cupric oxide monoclinic structure and the rock salt structure was observed with increasing concentrations of Mn and Sn, while the concentration of Cu simultaneously decreased in the precursors. The crystallite size decreased throughout the samples, reaching a minimum value of 9.8 nm at an equimolar ratio. Scanning electron microscopy further confirmed this downward trend and indicated an improvement in the quality of the film surfaces. According to the optical absorption measurements, the bandgap energy ranged from 2.68 to 3.44 eV. Interestingly, the sheet resistance of $\text{Cu}_{1-2x}\text{Mn}_x\text{Sn}_x\text{O}$ films dropped sharply from 5.24 k Ω /sq for CuO to 0.034 k Ω /sq for the film with a molar ratio of Cu:Mn:Sn being 34:33:33.

1. Introduction

Silicon-based thin-film transistors (TFTs) and related devices have been consumed the most in the semiconductor industry for a long time because of their high field-effect mobility, high optical transparency in the visible range, and high uniformity over large surfaces [1]. However, the poor electrical performance of amorphous Si TFTs and the low scalability and high fabrication costs of low-temperature polycrystalline Si TFTs present a bottleneck in using these materials for large high-resolution displays, despite their ability to easily control the electrical properties [2]. Fortunately, oxide TFTs are regarded as promising alternatives and have been extensively researched due to their high mobility, low off-current, high transparency, high uniformity, and simple fabricating methods [3]. In the literature, most oxide TFTs are based on n-type semiconductors. From typical pure binary systems such as ZnO [4], In_2O_3 [5], and SnO_2 [6], the advantage of ternary and quaternary multi-component cation systems has been investigated, including indium-zinc oxide [7], zinc-tin oxide [8], indium-zinc-tin oxide [9], and indium-gallium-tin oxide [10] thin films as the channel layer of TFTs.

Conversely, in the early stage, p-type oxides faced skepticism as potential candidates for TFT channels due to difficulties in producing high-quality thin films, achieving a sufficiently large on-off current ratio, and their low hole mobility [11]. Recently, research on p-type oxide semiconductors has gained significant attention due to the excellent results that have been published. Several typical p-type oxide semiconductors, including copper (I) oxide (CuO) [12], Cu_2O [11], NiO [13], and SnO_x [14], have been thoroughly investigated for TFT channel layer. Among these, CuO is the most extensively studied material owing to its non-toxicity, low-cost fabrication, and abundant availability [15]. Modifying the synthesis conditions, such as the technique used, the parameters of a specific technique, or doping other impurities into the crystal lattice of CuO thin films, has resulted in upgraded performance of CuO p-type channel TFTs [12,16–18].

As mentioned above, the multi-component approach employed in the field of n-type semiconductors could be leveraged to enhance the performance of p-channel TFTs. Numerous studies have been conducted in this regard. For example, Z.Q. Yao et al. [19] demonstrated the p-type CuAlO_2 via magnetron sputtering at a temperature of 940 °C and

* Corresponding author.

E-mail address: trinhbnq@vnu.edu.vn (B.N.Q. Trinh).

sputtering power of 120 W, accompanied by varying the working pressure and oxygen content. The highest obtained hole mobility was 39.5 cm²/Vs, with the optimized top-gate transistor exhibiting an on/off current ratio of about 8.0×10^2 and a field effect mobility of 0.97 cm²/Vs. Using solution processing, Nie et al. [20] fabricated the CuCrO₂ thin films using a two-step annealing process. The best TFT achieved an on/off current ratio of $\sim 10^5$ and a hole mobility of 0.59 cm²/Vs. Apart from the above materials, other copper oxide-based ternary and quaternary systems have been explored primarily for photocatalytic activity. Therefore, researching and applying multi-component p-type oxide semiconductors in the channel layer of TFTs is essential.

There are various techniques to prepare multi-component p-type oxide semiconductor thin films, such as magnetron sputtering [19], pulsed laser deposition, spin-coating [21], chemical vapor deposition [22], and oxygen plasma assisted molecular beam epitaxy [23]. Among vacuum-based routes, the spin-coating method has evident advantages, including simplicity, low-power and low-material consumption, easy control of components' content, and the ability to form thin films on flexible substrates under atmospheric pressure.

In this paper, we report our work on a quaternary p-type oxide material composed of Cu, Mn, and Sn using solution-processing and spin-coating methods. The choice of Cu-Mn-Sn-O system was first based on the outstanding performance of SnO_x- and CuO-channel TFTs compared to the other p-type metal oxide semiconductors [1]. Additionally, research on Sn-doped and Mn-doped CuO thin films has yielded promising results. Wu et al. [24] studied the influence of Sn impurities on the characteristics of Sn:CuO thin films. They obtained a thin film with a resistivity of 47.4 Ωcm and a carrier concentration of 2.14×10^{16} cm⁻³ at a 1.5 % Sn doping concentration. Compared to those of pristine CuO thin film reported in their study (108 Ωcm and 3.06×10^{15} cm⁻³), the positive effect of Sn doping on the electrical properties was evident. Rahaman et al. [25] observed an upward trend in the resistivity of Mn-doped CuO thin films, rising from 10.5 Ωcm at 0 % Mn doping to 28.6 Ωcm at 4 % doping. The highest value of carrier concentration was approximately 6.2×10^{17} cm⁻³ at a 2 % doping concentration, indicating significant improvement. Thus, taking advantage of typical p-type oxide semiconductor CuO, we incrementally increased the contents of Mn and Sn while concurrently reducing the content of Cu in the precursors to determine the impact of heavy substitution on the characteristics of the pristine CuO thin film. The crystal structure, surface morphology, optical bandgap energy, and electrical properties of fabricated Cu_{1-2x}Mn_xSn_xO thin films with $x = 0.05, 0.10, 0.15, 0.20, 0.25, 0.30$, and 0.33 were systematically scrutinized for evaluation purposes.

2. Experimental methods

2.1. Precursor preparation

Copper (II) acetate monohydrate (Cu(CH₃COO)₂·H₂O ≥99.0 %), manganese (II) acetate tetrahydrate (Mn(CH₃COO)₂·4H₂O ≥99.0 %), and tin (II) chloride dihydrate (SnCl₂·2H₂O ≥98.0 %) were used as starting materials for the cations. Initially, the salts were dissolved in pure ethanol solvent at various synthesis percentages (Table 1), followed by the addition of diethanolamine (DEA) as the stabilizer. The solutions were then heated at 75 °C for 60 min on a digital hot plate stirrer to form the molecular network. Finally, an amount of monoethanolamine (MEA) was added to the solutions to achieve complete dissolvability. Note that the total cation concentration in the precursor solutions was controlled at 0.25 mol/L, and the concentration of both DEA and MEA was kept at 0.5 mol/L for optimum conditions. Precursors of manganese and tin pure oxides were also prepared using the same route for reference purposes.

Table 1

Components' molar base of Cu_{1-2x}Mn_xSn_xO thin films under diverse synthesis conditions. Note that the molar basis of Mn and Sn is the same.

Sample labels	Nominal value of x	Molar basis (mol/L)	
		Cu	Mn and Sn
CuO	0.00	0.250	0.00
M1	0.05	0.225	0.013
M2	0.10	0.200	0.025
M3	0.15	0.175	0.038
M4	0.20	0.150	0.050
M5	0.25	0.125	0.063
M6	0.30	0.100	0.075
M7	0.33	0.085	0.083

2.2. Fabrication of Cu_{1-2x}Mn_xSn_xO thin films

Acetone, ethanol, deionized water, and an ultrasonic bath were used to clean commercial 22 × 22 mm² Deckglaser cover glasses to remove any organic contaminants. All the substrates were soaked in a 2 % HF solution for 60 s to eliminate the metal dust, as well as build up an H⁺ layer on the surfaces to improve the grip of the solution on the substrates. Subsequently, the substrates experienced three cycles of spin-coating (at a speed of 1500 rpm for 50 s) and drying (in ambient atmosphere at 90 °C for 7 min) processes to obtain the desired film thickness. Eventually, the coated Cu_{1-2x}Mn_xSn_xO films were annealed in ambient atmosphere at 500 °C for 30 min to form the crystalline structure.

2.3. Thin films characterization

The structural, morphological, chemical compositional, optical, and electrical properties of the films were analyzed. A PANalytical Empyrean diffractometer with parallel-beam Cu-K α radiation ($\lambda = 1.54056$ Å) was employed to investigate the crystal structure, scanning from 20° to 70° with a scanning speed of 0.03°/s. The surfaces of the films were inspected using a scanning electron microscope (SEM, JSM-IT100, Jeol) at 1 μm scale with a working distance of 12 mm and operated at an accelerating voltage of 15 kV. This was followed by chemical element analysis using the integrated energy dispersive spectroscopy (EDS) system (IT100LA, JEOL-made) at the same operating voltage. The optical properties were measured using a UV/VIS spectrophotometer (UV 2450-PC, Shimazu) in the wavelength range of 300 to 800 nm. The electrical resistivity and Hall voltage of the CuO-based quaternary thin films were determined using a four-probe (RM3000, Jandel) and a room-temperature Hall effect measurement system (Suimoto/SHI CH-202FF).

3. Results and discussion

3.1. Structural analysis

The x-ray diffraction (XRD) patterns of the multi-component Cu_{1-2x}Mn_xSn_xO oxide thin films ($x = 0.05, 0.10, 0.15, 0.20, 0.25, 0.30$, and 0.33) are shown in Fig. 1. For the CuO thin film, typical peaks were located at $2\theta = 35.54^\circ$ and 38.70° , corresponding to the (002) and (111) planes of the CuO monoclinic structure (JCPDS 00-045-0937) belonging to the C2/c space group. The superior intensities of the (002) and (111) peaks, accompanied by their ratios, indicate a tendency to form a polycrystalline system without any considerable secondary phases. This is consistent with previous reports on sol-gel-processed CuO thin films [26,27].

In samples M1 and M2, a similar pattern emerged, but with stronger peak intensities. No diffraction peaks corresponding to Cu, Mn, or Sn phases are evident in these XRD patterns, suggesting the complete substitution of Sn and Mn ions at Cu²⁺ sites within the lattice cells. We hypothesize that the ions involved could be Mn³⁺ and Sn⁴⁺, given their smaller ionic radii than that of Cu²⁺ (0.645, 0.690, and 0.720 nm [28],

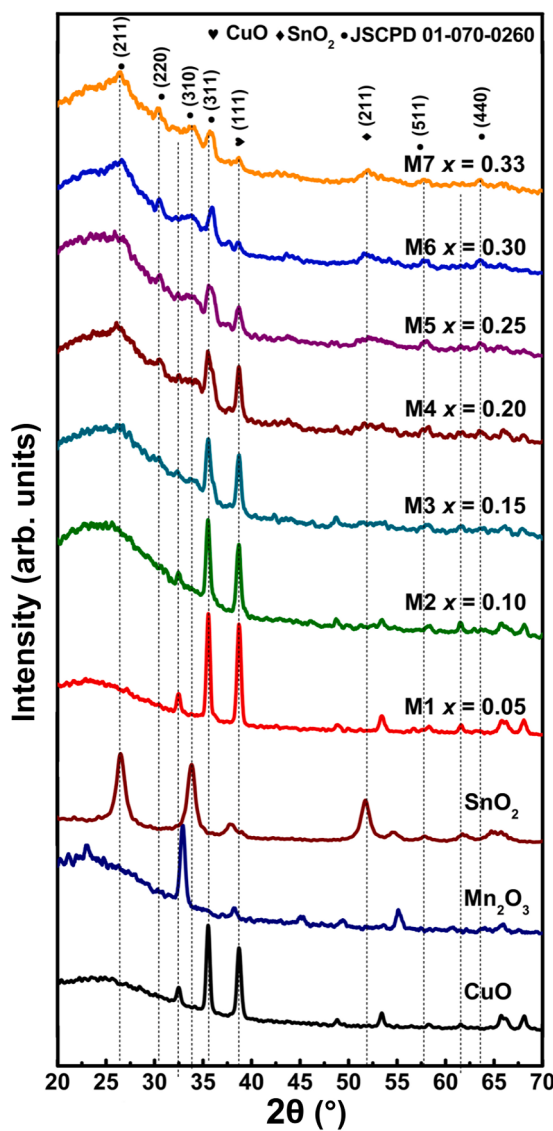


Fig. 1. XRD patterns of $\text{Cu}_{1-2x}\text{Mn}_x\text{Sn}_x\text{O}$ thin films on glass substrates at different atomic ratios, and those of CuO , Mn_2O_3 and SnO_2 thin films were also represented for comparison purposes.

respectively), facilitating substitution. However, when the portion of Cu^{2+} in the precursor is decreased, the CuO -monoclinic peaks in the diffractograms of the $\text{Cu}_{1-2x}\text{Mn}_x\text{Sn}_x\text{O}$ thin films are widened and relatively reduced in intensity. In particular, the films M3 ($x = 0.15$) and M4 ($x = 0.20$) exhibited two noticeable phenomena: (1) the existence of peaks at $2\theta = 25.95^\circ$ and 51.71° , which are well matched with the (110) and (211) standards of the SnO_2 phase; and (2) the appearance of the peaks at $2\theta = 30.57^\circ$ and 61.51° , which do not correspond to any phases associated with the three metal elements studied here. As the molar ratio of Sn^{4+} and Mn^{3+} in the precursor increased, the intensities of these additional peaks also increased. Moreover, a rightward shift of the peak (002) was observed at samples M5, M6, and M7. Tawfik et al. [29] proposed that compressive stress could lead to a high-angle shift, which concurs with this study, as the substitution of smaller ionic radii compared to host ions. As the degree of substitution increases, the compressive strain also increases, causing a shift in the diffraction angle position. In addition, except for the (111) peak at 38.65° and the peak (211) at 52.03° , which correspond to CuO and SnO_2 respectively, the XRD pattern of the M7 ($x = 0.33$) thin film is appropriate for the cubic structure belonging to the P4332 space group (JCPDS 01-007-0260).

This indicates a phase transition from monoclinic to cubic.

The $\text{Cu}_{1-2x}\text{Mn}_x\text{Sn}_x\text{O}$ crystallite sizes (D) were calculated using Scherrer's equation:

$$D = \frac{0.9\lambda}{\beta \cos \theta} \quad (1)$$

where λ is the exploited wavelength (1.5406 \AA), θ is the Bragg diffraction angle, and β is the full width at half maximum (FWHM) of the peak located at 2θ . We also considered the microstrain (ε) and the dislocation density (δ) of all the films, which were determined using the following formulas:

$$\varepsilon = \frac{\text{FWHM} \cos \theta}{4} \quad (2)$$

$$\delta = \frac{1}{D^2} \quad (3)$$

Table 2 presents the D , ε , and δ values calculated from the (002) peak (peak (311) for sample M7). The crystallite size, starting from 36.6 nm for the CuO thin film, gradually diminishes with increasing Mn and Sn content, reaching a minimum of 9.8 nm when the atomic ratio between Cu, Mn, and Sn is approximately equalized. Similar downward trends were observed in previous reports on doping elements with ionic radii smaller than those of host materials, resulting in the increase of compressive strain and subsequent reduction in the volume of unit cells [30,31]. This increase in compressive strain also affects the FWHM values, causing a discernible broadening of the angular peak width. This finding is corroborated by the proposal made by Hemathangam et al. [31], which indicates a correlation between compressive strain and FWHM broadening.

3.2. Morphological and chemically compositional analysis

The surface morphology of the multi-component $\text{Cu}_{1-2x}\text{Mn}_x\text{Sn}_x\text{O}$ oxide thin films is shown in **Fig. 2**. Increasing the Mn and Sn contents significantly improved the quality of the film surfaces. Specifically, while samples CuO , M1, M2, and M3 ($x = 0.00$, 0.05 , 0.10 , and 0.15) had surfaces with evenly distributed grains and pinholes, the other samples became denser and were entirely covered by grains without any pinholes. This transition from porous to non-porous states can enhance the electrical conductivity of thin films. The average particle size (D_{mean}) and standard deviation (ΔD) values were assessed using the ImageJ software and the Gaussian fitting function. As shown in **Fig. 3**, a declining trend is apparent despite the particle sizes derived by the ImageJ software surpassing those obtained through the Debye-Scherrer formula (285.91 to 76.61 nm). This inconsistency may arise from particle agglomeration, as suggested by Selbach et al. [32].

The atomic composition of the quaternary thin films was determined using EDS analysis at an operating voltage of 15 kV . During the measurement, only sample-related estimates, namely those for Oxygen, Copper, Manganese, Tin, and Potassium, were retained, as shown in the insert of **Fig. 4(a)**. To accurately compare these EDS results with the initial ratios in the precursors during preparation, the results were

Table 2
Microstructural parameters of $\text{Cu}_{1-2x}\text{Mn}_x\text{Sn}_x\text{O}$ thin films across varying x values.

Nominal value of x	$2\theta (\text{ }^\circ)$	FWHM (°)	D (nm)	$\varepsilon (\times 10^3)$	$\delta (\times 10^3)$
CuO 0.00	35.49	0.24	36.6	1.00	0.75
M1 0.05	35.53	0.33	26.3	1.37	1.45
M2 0.10	35.47	0.35	24.1	1.45	1.72
M3 0.15	35.54	0.35	24.1	1.45	1.72
M4 0.20	35.50	0.47	18.0	1.95	3.09
M5 0.25	35.83	0.71	11.9	2.95	7.06
M6 0.30	35.96	0.72	11.7	2.99	7.31
M7 0.33	35.80	0.86	9.8	3.57	10.41

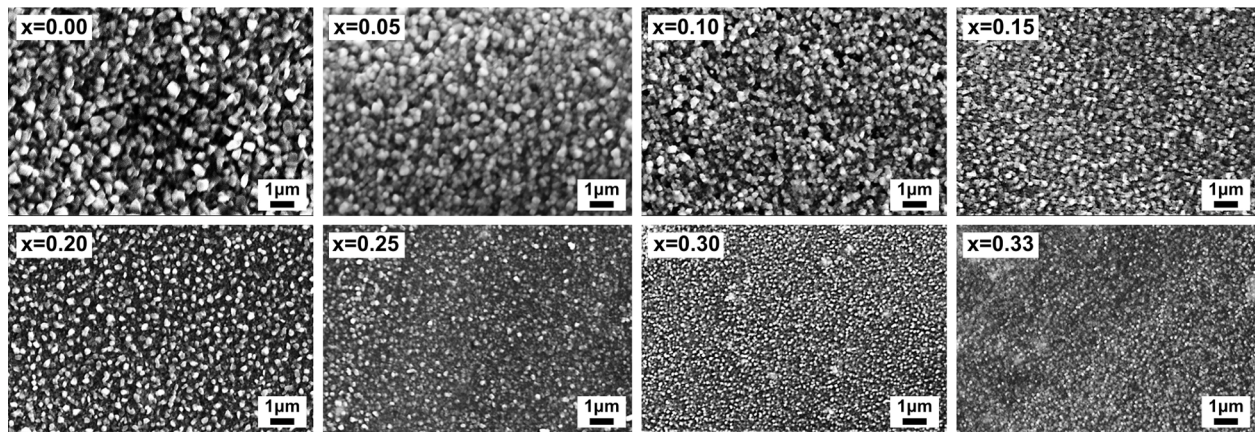


Fig. 2. SEM micrographs of Cu_{1-x}Mn_xSn_xO thin films with nominal values of x varying between 0 and 0.33.

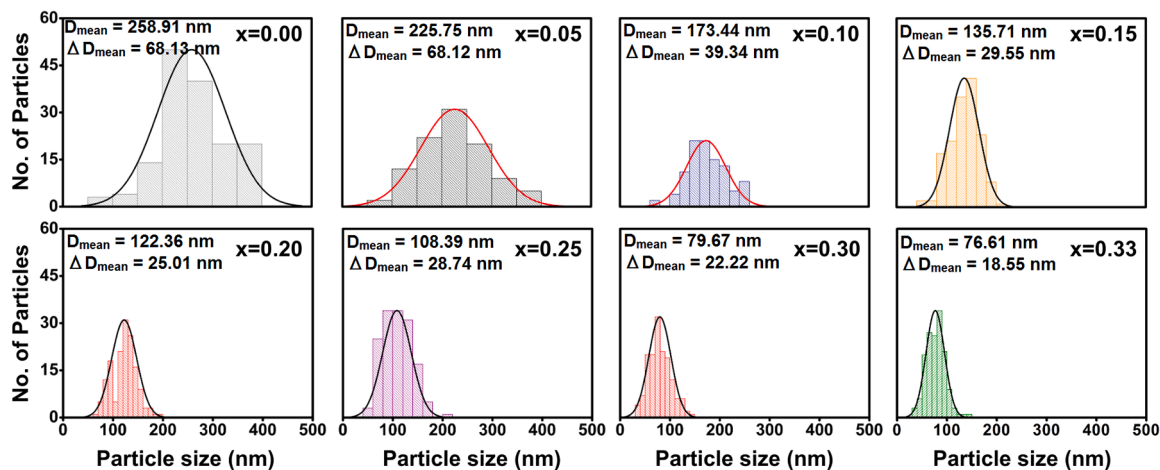


Fig. 3. Particle size of Cu_{1-x}Mn_xSn_xO thin films. Individual particle sizes were identified from SEM images using ImageJ software. The average particle size (D_{mean}) and standard deviation (ΔD) were calculated using the Gaussian fitting function.

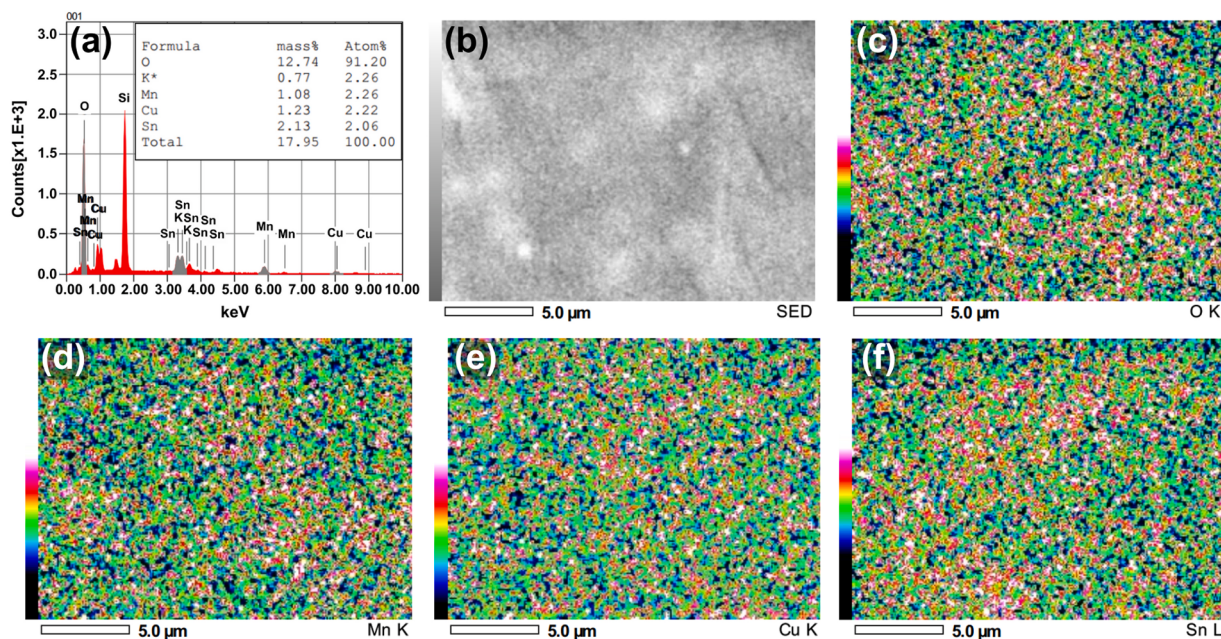


Fig. 4. The EDS mapping measurement of Cu_{1-x}Mn_xSn_xO thin film with x = 0.33. The insert of (a) indicates the corresponding compositional estimates.

normalized and are detailed in **Table 3**. It is apparent that the elemental contents do not perfectly match those of the precursors, with the estimates for Mn being more accurate than those for Sn. This inaccuracy could be attributed to the similarity in characteristic X-ray energy of the K-orbital of Potassium and the L-orbital of Tin (3.42 and 3.44 keV [33, 34], respectively), which may lead to errors in detecting and distinguishing these two elements during the EDS operation. As depicted in **Fig. 4(a)**, EDS peaks of Potassium and Tin mostly overlap in the range of 3.00 to 4.50 keV. **Fig. 4(b)** to (f) illustrate the mapping measurement result of sample M7 ($x = 0.33$), showing the uniform distribution of Cu, Mn, and Sn atoms on the surface of the film.

3.3. Optical property

The optical absorbance of all the thin films was measured using a UV-Vis spectrometer in the range of 300–800 nm, as shown in **Fig. 8(a)**. The optical bandgap energy can be obtained using Tauc's expression [35]:

$$(\alpha h\nu) = A(h\nu - E_g)^2 \quad (4)$$

where $h\nu$ is the radiation energy, α is the absorption coefficient, and A is the energy-independent constant of the material. **Fig. 5(a)** shows the $(\alpha h\nu)^2$ versus incident energy of photon ($h\nu$) plots for $\text{Cu}_{1-2x}\text{Mn}_x\text{Sn}_x\text{O}$ thin films. The direct optical bandgap energy values (E_g) were extrapolated from the linear portions of the curves, and are presented in **Table 4**. In the case of $x = 0.00$, corresponding to the CuO semiconductor, the calculated bandgap energy value is 2.68 eV, which is higher than that of bulk material and other publications using a sol-gel process. For example, Nguyen et al. [36] prepared thin films of CuO under similar conditions, indicating a bandgap energy of 2.1 eV. This discrepancy can be explained by the relationship between the grain size and the optical bandgap, as suggested by Öztas. According to Öztas, as the grain size increases, the energy gap may decrease because of the diminution of the quantum size effect [37]. In the study of Nguyen, the grain size of the CuO thin film was 46 nm, which is higher than that in this study (36 nm), leading to a narrower bandgap. Another reason for the expansion of the optical bandgap of CuO in this study could be the influence of the two stabilizers. Wannes et al. [38] found that thin film with DEA stabilizer possess the widest forbidden gap compared to those stabilized with MEA, ammonium hydroxide, and nitric acid. In this study, we utilized both MEA and DEA as stabilizers, which could result in the aforementioned expansion.

The variation in the optical bandgap of the remaining multi-component oxide thin films is shown in **Fig. 5(b)**. The bandgap energy values fluctuate in the following three stages when adding more Mn and Sn into the crystal lattice while concurrently decreasing the Cu content. In the initial stage, with Mn and Sn contents ranging from 0 to 15 % for each element, there was a gradual increase in the bandgap energy from 2.68 to 2.85 eV. These substitution levels might not be sufficient to induce a significant change in the optical characteristics of the oxide thin films, resulting in only marginal expansion of the bandgap energy. Subsequently, a remarkable escalation to 3.15 eV is observed when the content of Mn and Sn reaches 20 % ($x = 0.2$) for each substance, continuing to increase until reaching a peak of 3.44 eV at the sample M6,

with the atomic ratio between Cu, Mn, and Sn being 40:30:30. This result is in good agreement with the XRD and SEM results. The XRD pattern of sample M4 ($x = 0.20$) shows two SnO_2 peaks and two extraordinary peaks, while the surface of this sample shows noticeable improvements compared to the thin films of CuO ($x = 0.00$), M1 ($x = 0.05$), M2 ($x = 0.10$), and M3 ($x = 0.15$). All these changes could contribute to a drastic increase in the optical bandgap energy. Finally, the figure of bandgap energy significantly lowers to 3.11 eV at sample M7, with an approximately equimolar atomic ratio.

The expansion of the bandgap energy observed in this study can be ascribed to two other phenomena. Rao et al. [39] claimed that the increase in compressive strain drives the wider forbidden gap in semiconductors. As discussed, because the Mn^{3+} and Sn^{4+} ions have smaller ionic radii than Cu^{2+} , substitution could boost the intensity of compressive strain within the crystal lattice, thereby increasing the optical bandgap energy of $\text{Cu}_{1-2x}\text{Mn}_x\text{Sn}_x\text{O}$ multi-component oxides. Moreover, the Burstein-Moss effect, which describes a modification of the Fermi level when heavily doped impurities into structures of semiconductors, is considered a root cause for the expansion of forbidden gap [40]. Normally, the Fermi level (E_F) of the CuO semiconductor is located inside the gap between the conduction band and the valance band, as depicted in **Fig. 6(a)** and (b), constructed based on an electronic formation schematic proposed by Yang et al. [41]. For donor doping, the Fermi level can be calculated using the following formula:

$$E_F = E_i + kT \ln \frac{N_d}{n_i} \quad (5)$$

where E_i is the Fermi level of the intrinsic semiconductor, k is the Boltzmann constant, N_d is the donor atom concentration, and n_i is the intrinsic carrier concentration of the semiconductor [42]. According to this equation, as more impurities are doped into the crystal lattice, the Fermi level is likely to elevate to a higher energy level until it settles inside the conduction band, with all states below E_F being occupied. Owing to the Pauli exclusion principle, electrons can only occupy states above the Fermi level, causing a blueshift of the absorption edge, as shown in **Fig. 6(c)**. In common practice, research on doped oxides typically maintains a proportion of 100 % of host cations and introduces other atoms at relatively low concentrations. However, in this study, the concentration of Cu^{2+} ions gradually declines (corresponding to the decrease in the concentration of intrinsic carriers) along with the escalation of substituting carrier concentrations (Sn^{4+} and Mn^{3+} ions), leading to a considerable increase in the bandgap energy values. As mentioned earlier, E_g of the approximately equimolar thin film was lower than that of the $\text{Cu}_{0.4}\text{Mn}_{0.3}\text{Sn}_{0.3}\text{O}$ thin film, which could be the outcome of the phase transition. Khatun et al. [43] found that at different Ga doping concentrations, TiO_2 thin films have distinct structures, thereby varying the bandgap energy. The flatter slopes observed in the bandgap energy values of $\text{Cu}_{0.5}\text{Mn}_{0.25}\text{Sn}_{0.25}\text{O}$ and $\text{Cu}_{0.4}\text{Mn}_{0.3}\text{Sn}_{0.3}\text{O}$ thin films indicate saturation before undergoing a transition into a unique structure and altering the optical characteristics.

3.4. Electrical property

The influence of varying component concentrations on the sheet resistance of $\text{Cu}_{1-2x}\text{Mn}_x\text{Sn}_x\text{O}$ thin films was evaluated using a four-probe measurement system at room temperature. As shown in **Table 4**, the sheet resistance ranged from 5.240 k Ω /sq to 1.083 k Ω /sq for x values ranging from 0.00 (CuO) to 0.25 (M5). This represents a significant improvement in electrical conductivity compared to our previous report on CuO thin films, where the sheet resistance varied from 230 to 9 k Ω /sq [36]. Surprisingly, when the Mn and Sn contents increased further, the sheet resistance decreased sharply to 0.398 k Ω /sq for the thin film with $x = 0.30$, reaching a minimum of 0.034 k Ω /sq at an atomic ratio close to equimolar ($x = 0.33$). We believe that this enhancement could be the result of the combination of massive substitution, morphology-related

Table 3
Analysis of EDS results for $\text{Cu}_{1-2x}\text{Mn}_x\text{Sn}_x\text{O}$ thin films.

	Nominal value of x	Cu (at.%)	Mn (at.%)	Sn (at.%)
M1	0.05	0.91	0.05	0.04
M2	0.10	0.86	0.09	0.05
M3	0.15	0.75	0.12	0.13
M4	0.20	0.64	0.20	0.16
M5	0.25	0.51	0.23	0.26
M6	0.30	0.45	0.29	0.26
M7	0.33	0.34	0.35	0.31

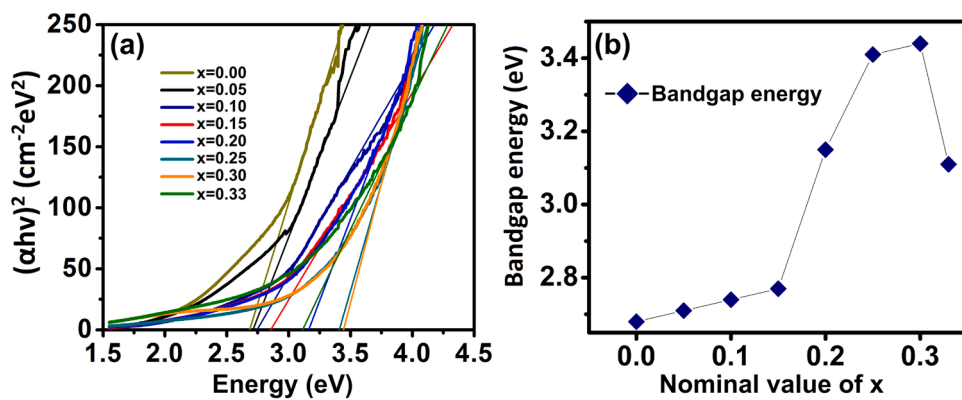


Fig. 5. The Tauc's plots (a) and the bandgap energy values plotted as a function of Mn and Sn percentage concentration (b).

Table 4

Electrical and optical characteristics for the Cu_{1-x}Mn_xSn_xO thin films. The sheet resistance was measured repeatedly at five spots on the surface, including the central point and four corners, and then the mean values were extracted. The error in this determination was found to be around ± 5 %.

Nominal value of x	E _g (eV)	Sheet resistance (kΩ/sq)	Absorption length (nm)	a-FOM (Ω ⁻¹ cm ⁻¹)	Type
CuO	0.00	2.68	5.240	50.5	9.64
M1	0.05	2.71	4.322	66.4	15.36
M2	0.10	2.77	3.979	66.1	16.61
M3	0.15	2.85	1.689	64.3	38.07
M4	0.20	3.15	1.111	55.7	50.13
M5	0.25	3.41	1.083	58.6	54.11
M6	0.30	3.44	0.398	57.9	145.48
M7	0.33	3.11	0.034	60.9	p

a-FOM: Absorption figure of merit for dark-surface oxide thin films, originally devised in our previous publication [36].

improvement, and phase transition.

In thin film research involving impurity doping, scientists typically vary the doping content from 0 to under 15 %. This usually leads to an increase in conductivity owing to the release of free electrons/holes when the impurities occupy the host ion sites [44,45]. However, conductivity does not always improve linearly and may fluctuate or peak before declining. Nesa et al. [46] used spray deposition to prepare Zn-doped CuO thin films with doping contents ranging from 0 to 6 at%. They acquired the lowest resistivity at 5 % doping, and increasing Zn concentration beyond 5 at% resulted in reduced conductivity due to the limitation in the solubility of Zn into the CuO lattice. Wu et al. [24] inferred an identical trend when Sn atoms were doped into the CuO

crystal lattice. The lowest resistivity was achieved at 1.5 at% doping concentration but increased again at 2.0 at% because of crystal defect formation from excessive Sn dopants. Carrier mobility followed the same pattern, influenced by fluctuating grain size and carrier concentration, that is, the increase in carrier concentration lowers the mobility, which can be attributed to upgraded ionized impurities scattering [47].

In this study, the concentration of host atoms (Cu) decreased with an increase in the number of additional atoms (Mn and Sn), thereby increasing the carrier concentration. This minimizes the possibility of excessive atoms owing to solubility limitations and reduces the effect of impurity scattering. Consequently, no significant factors within the semiconductors weaken the improvement in electrical conductivity. Even when impurity scattering prevails and carrier mobility declines, the increase in carrier concentration can surpass the decrease in mobility, thereby maintaining the conductivity enhancement [48]. The reduction in the electrical sheet resistance also aligns with the quality improvement of the film surfaces, as evidenced by the SEM images. Moreover, Suzuki et al. [49] suggested an inverse correlation between grain size and the conductivity of semiconducting thin films, with smaller grain sizes associated with better film conductivity. This aligns with the observed decrease in grain size in our study.

The third supposition, rooted in the phase transition, is supported by several reports demonstrating a positive effect on electrical conductivity due to the change from a monoclinic to cubic structure. F. Fujishiro's study on Ba₂(Fe_{1-x}In_x)₂O₅ revealed that the monoclinic-phase Ba₂Fe₂O₅ exhibited poorer conductivity compared to the cubic-phase of Ba₂(Fe_{1-x}In_x)₂O₅ where x ranged from 0.1 to 0.8 [50]. Similarly, Sato et al. investigated the correlation between the sintering temperature, crystal structure, and electrical properties of Ba₂Fe₂O_{5+δ} by varying the sintering temperature from 200 to 1100 °C [51]. They noticed that

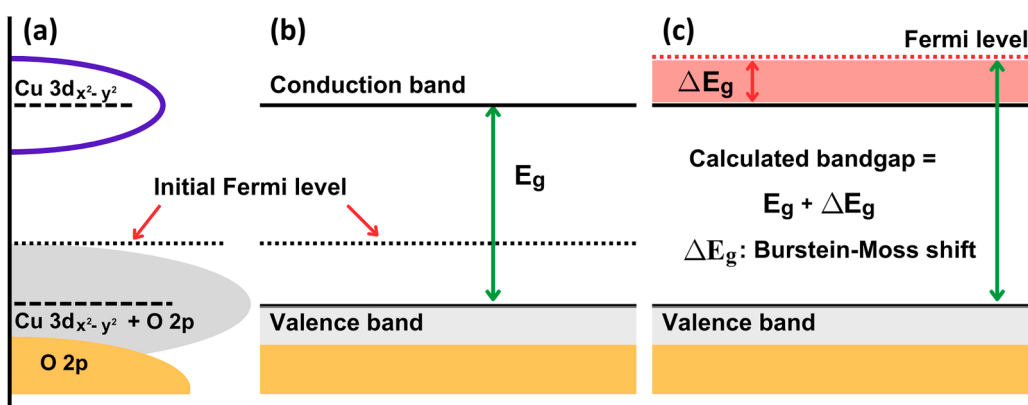


Fig. 6. The p-type semiconductor band structure before (a, b) and after being modified by the Burstein-Moss effect (c). The schematic depicted in (a) and (b) was reproduced from the study of J. Yang et al. [41].

below 800 °C, additional cubic peaks gradually emerged in addition to the main monoclinic phase peaks, inducing a steady increase in conductivity. Subsequently, at 900 °C, a pure cubic structure dominated, leading to a sudden improvement in electrical conduction. In our findings, the XRD patterns of samples M4 to M7 ($x = 0.20$ to 0.33) exhibited a phase transition similar to that observed in Sato's research, transitioning from a monoclinic structure to a rock salt phase, correlating with the sheet resistance decline. Therefore, despite the poorer crystallinity compared to samples M1 to M6 and the presence of two minor peaks of SnO_2 and CuO , the conductivity of sample M7 ($x = 0.33$) was not hindered, as evidenced by its lowest sheet resistance.

To determine the carrier type of sample M7, which has the lowest sheet resistance, Hall effect measurements were conducted at room temperature with a 0.45 T magnetic field, benefiting the Van der Pauw configuration. The voltage change across the sample in response to an applied magnetic field was assessed as a function of time. As shown in Fig. 7, the voltage is about $-1.77 \mu\text{V}$ before applying the magnetic field, and then increases to $-1.62 \mu\text{V}$ upon introducing the magnetic field. This observed increase of $0.15 \mu\text{V}$ signifies the potential difference induced by the perpendicular magnetic field, known as the Hall voltage (V_H). The positive value of V_H confirmed that sample M7 exhibited p-type semiconducting characteristics. Although the carrier concentration and mobility are not currently known, these parameters will be probed in the next step to evaluate the applicability of this material to thin-film transistors.

3.5. Evaluation of the absorption figure of merit

Fig. 8(a) illustrates the absorption spectra of $\text{Cu}_{1-2x}\text{Mn}_x\text{Sn}_x\text{O}$ films in the range of 300–800 nm. In addition, we used the global spectrum of sunlight from the American Society for Testing and Materials for photovoltaic performance evaluation. Ideally, when considering whether a material can be effective for light harvesting, its absorption spectra must match those of the solar flux. However, the substitution of Mn and Sn cations reduced the ability to absorb light in the range of 400–800 nm, which is the pivotal part of solar light source. Therefore, we took advantage of the absorption length L_a as a method to assess the effectiveness of conductive oxide thin films [36]:

$$\frac{1}{L_a} = \frac{\int_{E_g}^{\infty} \alpha(E) u_{ph}(E) dE}{\int_{E_g}^{\infty} u_{ph}(E) dE} \quad (6)$$

where $\alpha(E)$ is the absorption coefficient as a function of photon energy, and u_{ph} is the photon flux. In general, the L_a factor indicates the depth at which light can pass through a semiconductor material before being completely absorbed [52]. This differs from the transport length, which represents the average distance a photon travels before its direction is

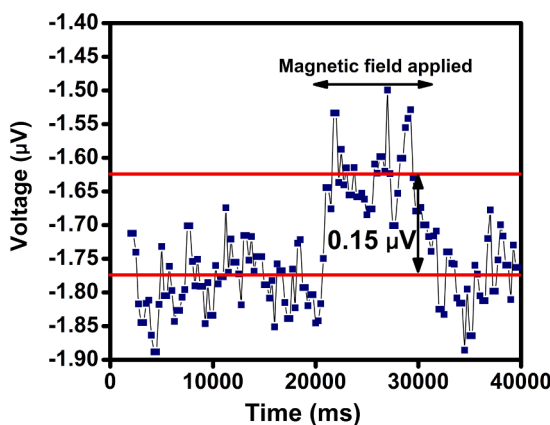


Fig. 7. The voltage variation across the $\text{Cu}_{1-2x}\text{Mn}_x\text{Sn}_x\text{O}$ ($x = 0.33$) thin film with the magnetic field application.

completely randomized. Thus, the term absorption length can be understood as the effective trapping of photons upon reaching the surface of semiconductor materials, with a higher absorption length indicating lower absorption effectiveness. By using Eq. (6), the respective values of L_a for thin films with different Mn and Sn contents were calculated and are listed in Table 4. The substitution of Mn and Sn leads to an increase in absorption length. Specifically, starting from 50.5 nm for the CuO films, the figure of absorption length rises significantly to 66.4 nm for the films with 90 % Cu^{2+} ions, then fluctuates around the range of 66.1 to 55.7 nm. The data for pristine CuO film is lower than that of our published reports [36,52], indicating the advancement of the fabricating process in terms of natural light harvesting.

To further examine the absorptivity of the films, the absorption figure of merit ($a\text{-FOM}$) factor was considered. This factor was originally introduced in our previous publication as an alternative to the conventional figure of merit for dark-surface oxide thin films [36].

$$a\text{-FOM} = \frac{L_a}{\rho d} \quad (7)$$

where ρ is the electrical resistivity and d is the film thickness. Fig. 8(b) shows the $a\text{-FOM}$ values (estimated from Eq. (7)) as a function of x values. The $a\text{-FOM}$ showed a proportional relationship with the contents of Mn and Sn, indicating that the higher the ratio of Mn (Sn) in the mixture, the higher the value of the absorption figure of merit. The influence of resistivity on the absorption figure of merit is recognizable. Regarding the sheet resistance of the M5 ($x = 0.25$) and M6 ($x = 0.30$) thin films, the drop from 1.083 to 0.398 $\text{k}\Omega/\text{sq}$ leads to a threefold surge from 54.11 to $145.48 \Omega^{-1}\text{cm}^{-1}$ in the figure of merit data. The highest recorded value was $176.67 \Omega^{-1}\text{cm}^{-1}$ for the film with a Cu:Mn:Sn ratio of 34:33:33. Table 5 compares the optoelectronic properties reported in several studies related to this work. It is evident that the sample $\text{Cu}_{1-2x}\text{Mn}_x\text{Sn}_x\text{O}$ with $x = 0.33$ possesses a much lower sheet resistance compared to that of solution-processed CuO , NiO , and Sn-doped CuO thin films, and even sputtered SnO_2 thin film. Regarding the absorption length and absorption figure of merits, $\text{Cu}_{0.34}\text{Mn}_{0.33}\text{Sn}_{0.33}\text{O}$ data surpasses those in our previous studies. This result highlights the remarkable advancement achieved by composing Cu, Mn, and Sn atoms in an equimolar ratio to form a quaternary oxide material, positioning it as a potential candidate for capturing natural light.

4. Conclusions

A comprehensive study of p-type oxide-semiconductors $\text{Cu}_{1-2x}\text{Mn}_x\text{Sn}_x\text{O}$ with $x = 0.05$, 0.10 , 0.15 , 0.20 , 0.25 , 0.30 , and 0.33 was carried out using a solution process. The XRD results revealed a phase transition from monoclinic to rock salt structure with increasing concentrations of additional Mn and Sn atoms. A decrease from 36.6 nm to 9.8 nm in crystallite size was observed, which is consistent with the trend of grain size estimated by SEM images (285.91–76.61 nm). Additionally, SEM images indicated a quality improvement of the film surfaces across all samples. The absorption edge exhibited a blueshift, with the maximum bandgap energy value being 3.44 eV, while a minimum sheet resistance of $34.47 \Omega/\text{sq}$ and a maximum absorption figure of merit of $176.67 \Omega^{-1}\text{cm}^{-1}$ were achieved for the thin film with an equimolar atomic ratio between Cu, Mn, and Sn. The achievements demonstrate significant potential for practical application in both electronics and optoelectronics. In particular, optimized thin film compositions are believed to enhance the performance of p-channel TFTs and their applicability in integrated circuits. Moreover, these materials have considerable potential as oxide materials for efficient solar-light harvesting.

CRediT authorship contribution statement

Dinh The Nam: Writing – original draft, Validation, Investigation.

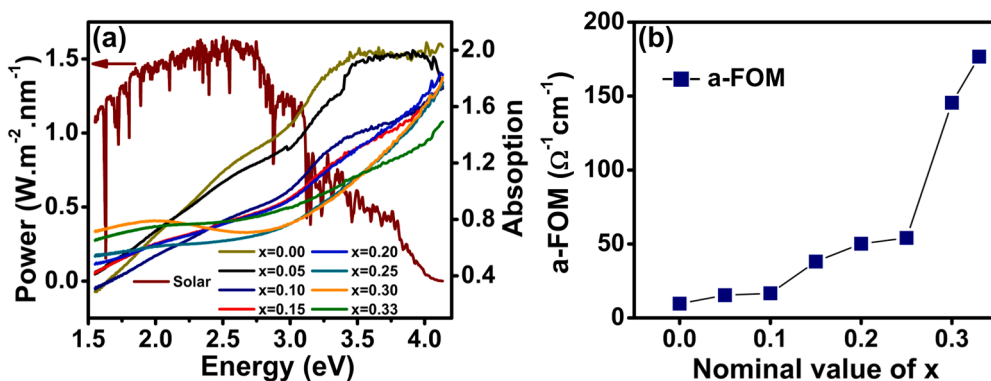


Fig. 8. Solar spectrum (brown curve) and absorbance of the Cu_{1-2x}Mn_xSn_xO thin films in the range of 300–800 nm (a) and the dependence of the absorption figure of merit on Mn and Sn concentration (b).

Table 5
Optoelectronic comparison of the p-type oxide thin films.

	E _g (eV)	Sheet resistance (Ω/sq)	Absorption length (nm)	a-FOM (Ω ⁻¹ cm ⁻¹)	Reference
NiO ^(*)	3.95	1.4 × 10 ⁵	—	—	[13]
SnO ₂ ^(*) a)	—	140	—	—	[53]
1.5 mol% Sn-doped CuO ^(*)	1.94	1.14 × 10 ⁶	—	—	[24]
CuO	2.10	9 × 10 ³	99.0	12.79	[36]
4 wt% Ni-doped CuO	1.88	2.07 × 10 ⁶	63.8	30.82	[52]
Cu _{0.34} Mn _{0.33} Sn _{0.33} O	3.11	34.47	60.9	176.67	This work

^a Prepared via magnetron sputtering.

* The value of the sheet resistance was normalized using data from the respective study.

Bui Nguyen Quoc Trinh: Writing – review & editing, Writing – original draft, Visualization, Validation, Supervision, Resources, Project administration, Methodology, Investigation, Funding acquisition, Formal analysis, Data curation, Conceptualization.

Declaration of competing interest

The authors declare that they have no known competing financial interests or personal relationships that could have appeared to influence the work reported in this paper.

Data availability

No data was used for the research described in the article.

References

- [1] Z. Ouyang, W. Wang, M. Dai, B. Zhang, J. Gong, M. Li, L. Qin, H. Sun, Research progress of p-Type oxide thin-film transistors, Materials (Basel) 15 (2022) 4781, <https://doi.org/10.3390/ma15144781>.
- [2] Y.J. Hung, C.T. Tang, T.H. Chen, T.H. Yen, M.J. Tsai, S.L. Lee, Low-loss polysilicon subwavelength grating waveguides and narrowband Bragg reflectors in bulk CMOS, Opt. Express 28 (2020) 7786–7798, <https://doi.org/10.1364/OE.381894>.
- [3] S. Yoon, S.J. Kim, Y.J. Tak, H.J. Kim, A solution-processed quaternary oxide system obtained at low-temperature using a vertical diffusion technique, Sci. Rep. 7 (2017) 43216, <https://doi.org/10.1038/srep43216>.
- [4] R.L. Hoffman, B.J. Norris, J.F. Wager, ZnO-based transparent thin-film transistors, Appl. Phys. Lett. 82 (2003) 733–735, <https://doi.org/10.1063/1.1542677>.
- [5] P.K. Nayak, M.N. Hedhili, D. Cha, H.N. Alshareef, High performance In₂O₃ thin film transistors using chemically derived aluminum oxide dielectric, Appl. Phys. Lett. 103 (2013) 033518, <https://doi.org/10.1063/1.4816060>.
- [6] V. Acharya, N. Pal, A. Sharma, U. Pandey, M. Suthar, P.K. Roy, S. Biring, B.N. Pal, Solution processed low operating voltage SnO₂ thin film transistor by using Li₂SnO₃/TiO₂ stacked gate dielectric, Mater. Sci. Eng. B 289 (2023) 116270, <https://doi.org/10.1016/j.mseb.2023.116270>.
- [7] E. Fortunato, P. Barquinha, A. Pimentel, L. Pereira, G. Gonçalves, R. Martins, Amorphous IZO TFTs with saturation mobilities exceeding 100 cm²/Vs, Phys. Status Solidi (RRL)-Rap. Res. Lett. 1 (2007) R34–R36, 10.1002/pssr.200600049.
- [8] S.J. Oh, C.J. Han, J.W. Kim, Y.H. Kim, S.K. Park, J.I. Han, J.W. Kang, M.S. Oh, Improving the electrical properties of zinc tin oxide thin film transistors using atmospheric plasma treatment, Electrochim. Solid-State Lett. 14 (2011) H354, 10.1149/1.3597660.
- [9] M.K. Ryu, S. Yang, S.-H.K. Park, C.S. Hwang, J.K. Jeong, High performance thin film transistor with cosputtered amorphous Zn-In-Sn-O channel: combinatorial approach, Appl. Phys. Lett. 95 (2009) 072104, <https://doi.org/10.1063/1.3206948>.
- [10] P. Ma, L. Du, Y. Wang, R. Jiang, Q. Xin, Y. Li, A. Song, Low voltage operation of IGZO thin film transistors enabled by ultrathin Al₂O₃ gate dielectric, Appl. Phys. Lett. 112 (2018) 023501, <https://doi.org/10.1063/1.5003662>.
- [11] K. Matsuzaki, K. Nomura, H. Yanagi, T. Kamiya, M. Hirano, H. Hosono, Epitaxial growth of high mobility Cu₂O thin films and application to p-channel thin film transistor, Appl. Phys. Lett. 93 (2008) 202107, 10.1063/1.3026539.
- [12] B.N.Q. Trinh, N. Van Dung, N.Q. Hoa, N.H. Duc, A. Fujiwara, Solution-processed cupric oxide p-type channel thin-film transistors, Thin Solid Films 704 (2020) 137991, <https://doi.org/10.1016/j.tsf.2020.137991>.
- [13] W. Xu, J. Zhang, Y. Li, L. Zhang, L. Chen, D. Zhu, P. Cao, W. Liu, S. Han, X. Liu, Y. Lu, P-type transparent amorphous oxide thin-film transistors using low-temperature solution-processed nickel oxide, J. Alloys Compd. 806 (2019) 40–51, <https://doi.org/10.1016/j.jallcom.2019.07.108>.
- [14] H.S. Jeong, M.J. Park, S.H. Kwon, H.J. Joo, H.I. Kwon, Highly sensitive and selective room-temperature NO₂ gas-sensing characteristics of SnO_x-based p-type thin-film transistor, Sens. Actuators B Chem. 288 (2019) 625–633, <https://doi.org/10.1016/j.snb.2019.03.046>.
- [15] A. Liu, S. Nie, G. Liu, H. Zhu, C. Zhu, B. Shin, E. Fortunato, R. Martins, F. Shan, In situ one-step synthesis of p-type copper oxide for low-temperature, solution-processed thin-film transistors, J. Mater. Chem. C 5 (2017) 2524–2530, <https://doi.org/10.1039/C7TC00574A>.
- [16] H. Lee, X. Zhang, B. Kim, J.H. Bae, J. Park, Effects of iodine doping on electrical characteristics of solution-processed copper oxide thin-film transistors, Materials (Basel) 14 (2021) 6118, <https://doi.org/10.3390/ma14206118>.
- [17] J.H. Bae, J.H. Lee, S.P. Park, T.S. Jung, H.J. Kim, D. Kim, S.W. Lee, K.S. Park, S.Y. Yoon, I.B. Kang, H.J. Kim, Gallium doping effects for improving switching performance of p-type copper (II) oxide thin-film transistors, ACS Appl. Mater. Interfaces 12 (2020) 38350–38356, <https://doi.org/10.1021/acsami.0c09243>.
- [18] S. Baig, P. Kumar, J. Ngai, Y. Li, S. Ahmed, Yttrium doped copper (II) oxide hole transport material as efficient thin film transistor, ChemPhysChem 21 (2020) 895–907, <https://doi.org/10.1002/cphc.202000005>.
- [19] Z.Q. Yao, B. He, L. Zhang, C.Q. Zhuang, T.W. Ng, S.L. Liu, M. Vogel, A. Kumar, W.J. Zhang, C.S. Lee, S.T. Lee, X. Jiang, Energy band engineering and controlled p-type conductivity of CuAlO₂ thin films by nonisovalent Cu-O alloying, Appl. Phys. Lett. 100 (2012) 062102, <https://doi.org/10.1063/1.3683499>.

- [20] S. Nie, A. Liu, Y. Meng, B. Shin, G. Liu, F. Shan, Solution-processed ternary p-type CuCrO₂ semiconductor thin films and their application in transistors, *J. Mater. Chem. C* 6 (2018) 1393–1398, <https://doi.org/10.1039/C7TC04810F>.
- [21] S.Y. Kim, J.H. Lee, J.J. Kim, Y.W. Heo, Preferential growth orientations of CuCrO₂ films grown by pulsed laser deposition, *Curr. Appl. Phys.* 12 (2012) S123–S126, <https://doi.org/10.1016/j.cap.2012.05.010>.
- [22] P.L. Popa, J. Crépellière, R. Leturcq, D. Lenoble, Electrical and optical properties of Cu–Cr–O thin films fabricated by chemical vapour deposition, *Thin Solid Films* 612 (2016) 194–201, <https://doi.org/10.1016/j.tsf.2016.05.052>.
- [23] D. Shin, J.S. Foord, R.G. Egddell, A. Walsh, Electronic structure of CuCrO₂ thin films grown on Al₂O₃(001) by oxygen plasma assisted molecular beam epitaxy, *J. Appl. Phys.* 112 (2012) 113718, <https://doi.org/10.1063/1.4768726>.
- [24] J. Wu, K.S. Hui, K.N. Hui, L. Li, H.H. Chun, Y.R. Cho, Characterization of Sn-doped CuO thin films prepared by a sol-gel method, *J. Mater. Sci.: Mater. Electron.* 27 (2016) 1719–1724, <https://doi.org/10.1007/s10854-015-3945-8>.
- [25] R. Rahaman, M. Sharmin, J. Podder, Band gap tuning and p to n-type transition in Mn-doped CuO nanostructured thin films, *J. Semicond.* 43 (2022) 012801, <https://doi.org/10.1088/1674-4926/43/1/012801>.
- [26] M. Dhaouadi, M. Jlassi, I. Sta, I.B. Miled, G. Mousdis, M. Kompitsas, W. Dimassi, Physical properties of copper oxide thin films prepared by sol-gel spin-coating method, *Am. J. Phys. Appl.* 6 (2018) 43–50, <https://doi.org/10.11648/j.apja.20180602.13>.
- [27] Y.F. Lim, C.S. Chua, C.J.J. Lee, D. Chi, Sol-gel deposited Cu₂O and CuO thin films for photocatalytic water splitting, *Phys. Chem. Chem. Phys.* 16 (2014) 25928–25934, <https://doi.org/10.1039/c4cp03241a>.
- [28] R.D. Shannon, Revised effective ionic radii and systematic studies of interatomic distances in halides and chalcogenides, *Acta Crystallogr. Sec. A: Found. Adv.* 32 (1976) 751–767, <https://doi.org/10.1107/S0567739476001551>.
- [29] W.Z. Tawfiq, Z.S. Khalifa, M.S. Abdel-wahab, A.H. Hammad, Sputtered cobalt doped CuO nano-structured thin films for photoconductive sensors, *J. Mater. Sci.: Mater. Electron.* 30 (2019) 1275–1281, <https://doi.org/10.1007/s10854-018-0395-0>.
- [30] S. Saravanan Kumar, R. Chandramohan, R. Premarani, J.J. Devadasan, J. Thirumalai, Studies on dilute magnetic semiconducting co-doped CDS thin films prepared by chemical bath deposition method, *J. Mater. Sci.: Mater. Electron.* 28 (2017) 12092–12099, <https://doi.org/10.1007/s10854-017-7022-3>.
- [31] S. Hemathangam, G. Thanapathy, S. Muthukumaran, Influence of Mn doping on structural, optical and photoluminescence properties of Cd_{0.98}Co_{0.02}S thin films by chemical bath deposition method, *J. Mater. Sci.: Mater. Electron.* 27 (2016) 1791–1798, <https://doi.org/10.1007/s10854-015-3955-6>.
- [32] S.M. Selbach, T. Tybell, M.A. Einarsrud, T. Grande, Size-dependent properties of multiferroic BiFeO₃ nanoparticles, *Chem. Mater.* 19 (2007) 6478–6484, <https://doi.org/10.1021/cm071827w>.
- [33] S.H. Chew, S.L. Yap, C.S. Wong, X-Ray spectroscopic measurements from copper and tin vacuum spark plasmas, *AIP Conf. Proc.* 1017 (2008) 335–340, <https://doi.org/10.1063/1.2940655>.
- [34] J. Valasek, X-Ray spectroscopic data in regard to the electronic energy bands in potassium and sodium chlorides, *Phys. Rev.* 53 (1983) 274, 10.1103/PhysRev.53.274.
- [35] N. Jhansi, D. Balasubramanian, R. Raman, Investigation on structural, optical and electrical behaviours of Sn doped copper oxide thin films and fabrication of diode, *J. Mater. Sci.: Mater. Electron.* 34 (2023) 1369, <https://doi.org/10.1007/s10854-023-10623-3>.
- [36] H.Q. Nguyen, D. Van Nguyen, A. Fujiwara, B.N.Q. Trinh, Solution-processed CuO thin films with various Cu²⁺ ion concentrations, *Thin Solid Films* 660 (2018) 819–823, <https://doi.org/10.1016/j.tsf.2018.03.036>.
- [37] M. Oztas, Influence of grain size on electrical and optical properties of InP films, *Chin. Phys. Lett.* 25 (2008) 4090, <https://doi.org/10.1088/0256-307X/25/11/069>.
- [38] H.B. Wannes, R.B. Zaghouani, R. Ouertani, A. Araújo, M.J. Mendes, H. Aguas, E. Fortunato, R. Martins, W. Dimassi, Study of the stabilizer influence on the structural and optical properties of sol-gel spin coated zinc oxide films, *Mater. Sci. Semicond. Process.* 74 (2018) 80–87, <https://doi.org/10.1016/j.mss.2017.10.017>.
- [39] T.P. Rao, M.C.S. Kumar, S.A. Angayarkanni, M. Ashok, Effect of stress on optical band gap of ZnO thin films with substrate temperature by spray pyrolysis, *J. Alloys Compd.* 485 (2009) 413–417, <https://doi.org/10.1016/j.jallcom.2009.05.116>.
- [40] F.K. Shan, B.I. Kim, G.X. Liu, Z.F. Liu, J.Y. Sohn, W.J. Lee, B.C. Shin, Y.S. Yu, Blueshift of near band edge emission in Mg doped ZnO thin films and aging, *J. Appl. Phys.* 95 (2004) 4772–4776, <https://doi.org/10.1063/1.1690091>.
- [41] J. Yang, W. Yin, B. Zhou, A. Cui, L. Xu, D. Zhang, W. Li, Z. Hu, Composition dependence of optical properties and band structures in p-type Ni-doped CuO films: spectroscopic experiment and first-principles calculation, *J. Phys. Chem. C* 123 (44) (2019) 27165–27171, <https://doi.org/10.1021/acs.jpcc.9b08604>.
- [42] J.P. Colinge, C.A. Colinge, *Physics of Semiconductor Devices*, Kluwer Academic Publishers, New York, 2002, p. 37.
- [43] N. Khatun, S. Tiwari, C.P. Vinod, C.M. Tseng, S.W. Liu, S. Biring, S. Sen, Role of oxygen vacancies and interstitials on structural phase transition, grain growth, and optical properties of Ga doped TiO₂, *J. Appl. Phys.* 123 (2018) 245702, <https://doi.org/10.1063/1.5027672>.
- [44] F. Lin, C. Gao, X. Zhou, W. Shi, A. Liu, Magnetic, electrical and optical properties of p-type Fe-doped CuCrO₂ semiconductor thin films, *J. Alloys Compd.* 581 (2013) 502–507, <https://doi.org/10.1016/j.jallcom.2013.07.160>.
- [45] H.Z. Asl, S.M. Rozati, Spray deposition of n-type cobalt-doped CuO thin films: influence of cobalt doping on structural, morphological, electrical, and optical properties, *J. Electron. Mater.* 49 (2020) 1534–1540, 10.1007/s11664-019-07858-4.
- [46] M. Nesa, M. Sharmin, K.S. Hossain, A.H. Bhuiyan, Structural, morphological, optical and electrical properties of spray deposited zinc doped copper oxide thin films, *J. Mater. Sci.: Mater. Electron.* 28 (2017) 12523–12534, 10.1007/s10854-017-7075-3.
- [47] W. Guan, L. Zhang, C. Wang, Y. Wang, Theoretical and experimental investigations of the thermoelectric properties of Al-, Bi- and Sn-doped ZnO, *Mater. Sci. Semicond. Process.* 66 (2017) 247–252, <https://doi.org/10.1016/j.mss.2017.03.027>.
- [48] F. Lin, C. Gao, Z. Zhou, W. Shi, A. Liu, Magnetic, electrical and optical properties of p-type Fe-doped CuCrO₂ semiconductor thin films, *J. Alloys Compd.* 581 (2013) 502–507, <https://doi.org/10.1016/j.jallcom.2013.07.160>.
- [49] T. Suzuki, I. Kosacki, H.U. Anderson, P. Coloban, Electrical conductivity and lattice defects in nanocrystalline cerium oxide thin films, *J. Am. Ceram. Soc.* 84 (2001) 2007–2014, <https://doi.org/10.1111/j.1151-2916.2001.tb00950.x>.
- [50] F. Fujishiro, Electrical conductivity of cubic perovskite Ba₂(Fe_{1-x}In_x)₂O₅ with disordered oxygen vacancies, *Mater. Chem. Phys.* 153 (2015) 5–8, <https://doi.org/10.1016/j.matchemphys.2015.01.022>.
- [51] T. Sato, T. Okiba, K. Shozugawa, M. Matsuo, F. Fujishiro, E. Niwa, T. Hashimoto, Dependence of crystal structure, phase transition temperature, chemical state of Fe, oxygen content and electrical conductivity of Ba_{2-x}LaxFe₂O_{5+δ} (x = 0.00–0.15) on La content, solid state ion. 290 (2016) 71–76, <https://doi.org/10.1016/j.ssi.2016.03.019>.
- [52] N. Van Loi, L.T.N. Mai, N.H. Luong, B.N.Q. Trinh, Enhancing the absorption figure of merit on solution-based CuO thin films by Ni doping, *Opt. Mater.: X* 19 (2023) 100246, <https://doi.org/10.1016/j.omx.2023.100246>.
- [53] A.Q. Duong, H.P. Dang, L. Le, Studying and fabricating optical, electrical, and structural properties of p-type Al- and N- co-doped SnO₂ (ANTO) films and investigating the photo-electro effect of p-ANTO/n-Si heterojunctions, *J. Photochem. Photobiol. A: Chem.* 390 (2020) 112334, <https://doi.org/10.1016/j.jphotochem.2019.112334>.